Cancer Nanotechnology

RESEARCH Open Access

Mesoporous silica nanoparticles boost aggressive cancer response to hydrophilic chlorin e6-mediated photodynamic therapy

Sara A. Abdel Gaber[1*], Herbert Stepp[2,3], Mahmoud H. Abdel Kader[4] and Mika Lindén[5]

*Correspondence:
sara_mohamed@nano.kfs.edu.eg

[1] Nanomedicine Department, Institute of Nanoscience and Nanotechnology, Kafrelsheikh University, Kafrelsheikh 33516, Egypt
[2] Laser Forschungslabor, LIFE Center, University Hospital, LMU Munich, Fraunhoferstr. 20, 82152 Planegg, Germany
[3] Department of Urology, University Hospital, LMU Munich, Marchioninistr. 15, 81377 Munich, Germany
[4] European universities in Egypt (EUE),R3, New Administrative Capital, next to the Olympic City, Cairo, Egypt
[5] Institute for Inorganic Chemistry II, Ulm University, Albert-Einstein-Allee 11, 89081 Ulm, Germany

Abstract

Background: Chlorin e6 trisodium salt (Ce6) is a newly developed hydrophilic photosensitizer designed to mediate anticancer photodynamic therapy (PDT). The response of different cancer types and strategies to boost anticancer efficiency of Ce6-PDT are poorly studied.

Objectives: This study aimed to investigate the response of different cancer types to Ce6-PDT, identify the unresponsive ones, and develop a nanosystem for response enhancement.

Methods: Sk-Br-3, MCF-7, U87, and HF-5 cells were tested in 2D cell cultures. Ce6 uptake, PDT-mediated phototoxicity, ROS production, caspase 3/7 levels, and cell death mode were examined. Furthermore, U87 spheroids were treated with Ce6-PDT. Mesoporous silica nanoparticles (MSN) were synthesized and loaded with Ce6. Cellular uptake and phototoxicity of MSN-Ce6 were compared to free Ce6 in vitro and in vivo.

Results: Ce6 was detectable in the cell cytoplasm within 15 min. U87 cells showed the highest Ce6 cellular uptake. Upon Ce6-PDT, U87 cells were the most responsive ones with an 11-fold increase in ROS production. Here, 5 µM Ce6 and 4 J/cm^2 were enough to reach IC50. Ce6-PDT induced both necrotic and caspase-dependent apoptotic cell death and 75% reduction of spheroids volume. Also, MCF-7 and HF-5 cells responded well to Ce6-PDT treatment. Sk-Br-3 breast cancer cells, on the other hand, were the least responsive ones with 80% viability after treatment (5 µM Ce6, 8 J/cm^2). However, MSN-Ce6 conjugates increased Sk-Br-3 cellular uptake of Ce6 sevenfold decreasing the IC50 irradiation dose by an order of magnitude. In a very aggressive breast cancer rat model, MSN-Ce6-PDT treatment led to suppression of tumor volume by 50% and elevation of both Bax and caspase 3 by 90% compared to the control while the corresponding values for Ce6-PDT were 30% and 70%, respectively.

Conclusion: The newly developed hydrophilic chlorin and even more its MSN conjugate show high activities in anticancer PDT.

Keywords: Chlorin e6 trisodium salt, Photodynamic therapy, Mesoporous silica nanoparticles, Anticancer, Caspase-dependent apoptosis

Introduction

Photodynamic therapy (PDT) is a local treatment that combines a photosensitizer (PS), cellular oxygen, and light. The illumination step triggers a sequence of photochemical reactions that generate deleterious reactive oxygen species (ROS). The latter may mediate apoptotic/necrotic/autophagic cell death, cessation of blood flow, and immunostimulation (Abdel Gaber 2017). Some PSs, such as 5- aminolevulinic acid (5-ALA), have gained approval for clinical applications (Peng et al. 1997). 5-ALA is a prodrug for the photosensitizer protoporphyrin IX (PPIX) and is approved for the treatment of actinic keratosis. Furthermore, it is intensively investigated for the treatment of different types of cancer such as glioblastoma (Müller et al. 2020), breast cancer (Guney Eskiler et al. 2020) and hepatocellular carcinoma (Ozten et al. 2022).

Chlorin e6 (Ce6) is a PS that is still in the pre-clinical and early clinical phases. It is one of the hydrophobic porphyrin derivatives with an absorption maximum of 665 nm granting deep tissue penetration. In its native form, Ce6 is rather hydrophobic and therefore has limited bioavailability. However, chemical modifications were applied to enhance its hydrophilicity. Conjugation with amino acid moieties, exemplified by aspartate lead to the formation of mono L-aspartyl Ce6, commercially known as Laserphyrin®, which is approved in Japan for the treatment of glioma and esophageal cancer (Kobayashi et al. 2022; Yano et al. 2021). Furthermore, complexation with surfactants such as polyvinylpyrrolidone in a 1:1 (w/w) dilution was also conducted in order to diminish the aggregation and to enhance the solubility (Hädener et al. 2015; Isakau et al. 2008). A simpler approach was the formation of a trisodium salt of the pure Ce6, commercially known as Fotolon®. It is readily soluble in aqueous medium, and has shown good PDT efficiency in the treatment of glioma (Abdel Gaber et al. 2018), onychomycosis (Yasin et al. 2022), keratitis (Wu et al. 2017) and *Helicobacter pylori* (Hüttenberger et al. 2017; Simon et al. 2014). However, the susceptibility of other cancer types to Ce6-PDT is not adequately studied.

In our previous study (Abdel Gaber et al. 2018), the relationship between serum protein concentration present at the in vitro level in fetal calf serum (FCS) and Ce6 cellular uptake was studied. The model was an engineered human glioblastoma multiforme cell line over-expressing the efflux pump ABCG2 upon induction to represent the stem-like sub-population of cancer cells. Ce6—in contrast to 5-ALA-induced PPIX—tended to bind to proteins after delivery. So, only after saturation of FCS-binding, efficient cellular uptake of Ce6 could take place. The role of ABCG2 was rather on the efflux side and modified PPIX more than Ce6. The relationship between FCS concentration and Ce6 cellular uptake using standard cancer cell lines was not investigated. Studying this relationship could optimize Ce6 protocol in terms of dosing regimen and administration route for diagnostic and therapeutic purposes.

Conjugating the PS with nanoparticles (NPs) is a common strategy to enhance the PDT therapeutic response (Mfouo-Tynga et al. 2021; Abdel Gaber and Fadel 2023). Silica-based NPs, including Stöber and mesoporous silica nanoparticles (MSN), are known for their facile synthesis, straightforward surface modification, and biocompatibility (Mamaeva et al. 2013), and have therefore attracted interest as PS carriers (Couleaud et al. 2010). A previous attempt with pure Ce6 reported a considerably low loading degree of 23 µg Ce6/mg silica NPs when Ce6 was covalently bound

to amino-functionalized Stöber NPs. Although the conjugate led to an improvement in PDT efficiency in vitro when compared to free Ce6, irradiation intensities as high as 60 J/cm^2 were needed to reach IC50 for breast cancer MDA-MB-231 cells (Bharathiraja et al. 2017). In another in vitro study, Ce6 was covalently attached to amino-functionalized silica NPs (Youssef et al. 2018). The reported Ce6 loading degree was only 6.5 µg/mg. Notably, already the bare silica NPs killed 30% of the glioblastoma cells, indicating that these particles were cytotoxic.

This study aimed to assess the PDT efficiency of the water-soluble trisodium salt of Ce6 in treating breast and glioma cancers compared to 5-ALA to better position it with respect to the FDA approved PS. Cancer types were ordered in terms of responsiveness and a third-generation PS developed by covalently conjugating Ce6 to MSN was tested for its ability to improve the therapeutic response in the least responsive cancer model. Bioassessments were conducted using human cell lines, 3D cellular spheroids, and an established cancer animal model.

Materials and methods

Materials

5-Aminolevulinic hydrochloride acid (5-ALA) was purchased from Medac GmbH, Hamburg, Germany. Chlorin e6 trisodium salt (Ce6) was a kind gift from Synverdis GmbH, Heidelberg, Germany. Basic fibroblast growth factor, Cell Titer Blue (CTB), and epidermal growth factor were purchased from Promega, Mannheim, Germany. 1-Ethyl-3-(3-dimethylaminopropyl) carbodiimide (EDC), N-hydroxysuccinimide (NHS), cetyltrimethylammonium bromide (CTAB), trimethylbenzene (TMB), tetraethylorthosilicate (TEOS), dimethyl sulfoxide (DMSO) and 3-aminopropyltriethoxysilane (APTES) were purchased from Sigma Aldrich, Germany, and used as received. Dulbecco's modified Eagle's medium (DMEM), DMEM F-12, McCoy's medium, fetal calf serum (FCS), phosphate buffer saline (PBS), and penicillin/streptomycin mixture were purchased from Biochrom AG, Berlin, Germany.

Synthesis of mesoporous silica nanoparticles (MSN)

Amino-functionalized MSN were synthesized following our previously published protocol using cetyltrimethylammonium bromide (CTAB) as the porogen (Rosenholm et al. 2009) with the exception that 10 mol-% of the silica source tetraethylorthosilicate (TEOS) was substituted by 3-aminopropyltriethoxysilane (APTES). Furthermore, trimethylbenzene (TMB) was added as a pore swelling agent ($n_{TMB}/n_{CTAB} = 2.5$). After the synthesis, the surfactant was removed by extraction in acidic ethanol, and the particles were dried under vacuum at 60 °C.

Synthesis of MSN-Ce6 conjugate

Ce6 was activated by 24-h reaction with 1.5 molar equivalent of 1-ethyl-3-(3-dimethylaminopropyl) carbodiimide (EDC), N-hydroxysuccinimide (NHS), in the presence of 1.5 mL anhydrous dimethyl sulfoxide (DMSO). MSN in phosphate buffer saline (PBS) was mixed with Ce6 at 1:5 wt/wt for 24 h. For conjugate collection, the mixture was centrifuged for 20 min at 7,000 g, and NPs were washed 3 times in PBS. Supernatants were

collected and the concentration of Ce6 was quantified spectrophotometrically at 405 nm (Bharathiraja et al. 2017). The entrapment efficiency was calculated using Eq. (1) and the loading efficiency was calculated using Eq. (2).

$$\text{Entrapment efficiency (\%)} = (\text{Ce6}_{\text{total}} - \text{Ce6}_{\text{unbound}})/\text{Ce6}_{\text{total}} \times 100 \quad (1)$$

$$\text{Loading efficiency (\%)} = (\text{Ce6}_{\text{total}} - \text{Ce6}_{\text{unbound}})/\text{weight of NPs} \times 100 \quad (2)$$

Characterization of the NPs and synthesized conjugate

The morphology of the synthesized NPs was studied by transmission electron microscopy (Jeol 1200 (Jeol, Germany) using HT voltage of 120 kV and beam current of 65 µA), and the pore size was determined by nitrogen sorption at −196 °C (Quantachrome Autosorb-1) and calculated using the NLDFT kernel developed for cylindrical pores, zeta-potential measurements were performed using a Zetasizer NanoZS Zen3600 setup (Malvern Panalytical, Germany) in aqueous KCl solutions (1 mM, particle concentration: 0.1 mg/mL). Fourier transmission infrared (FTIR) spectroscopy was conducted (Model no. 4000, JASCO, Japan) on Ce6, NPs, and conjugate with a range of 400–4000 cm^{-1} using KBr pellets.

Ce6 release kinetics from MSN

MSN-Ce6 (1 mg of MSN-Ce6 conjugate/mL, at room temperature) was sonicated in PBS at a pH of 7.4 or pH of 5.5 for 10 min. Mixtures were left stirring at room temperature at 600 rpm. At different time intervals over 24 h, aliquots of the mixture were withdrawn and replaced with fresh PBS of the same pH to maintain the volume. The concentration of Ce6 was measured spectrophotometrically at 405 nm and data were presented as cumulative Ce6 release % against the different time points (Couleaud et al. 2010).

Cell culture

Human breast cancer cell line (MCF-7), human glioblastoma cell line (U87), and human normal fibroblasts (HF-5) were cultured in Dulbecco's modified Eagle's medium (DMEM) medium. The human breast cancer cell line (Sk-Br-3) was cultured in McCoy's medium. All media were supplied with 10% fetal calf serum (FCS), 100 µg/mL non-essential amino acids, and 1 mM sodium pyruvate. The antibiotic mixture of 100 U/mL penicillin and 100 µg/mL streptomycin was added to assure having an aseptic medium. Cells were cultured at 37 °C in a humidified atmosphere supplied with 5% CO_2.

Quantification of cellular uptake by flow cytometry

A FACS Calibur flow cytometer (BD Biosciences) was used, and data were collected for 10,000 cells and analyzed using Flowing Software 2.5.1 (Turku Center for Biotechnology, Turku University, Finland). The Geometrical means (Geomean) of the respective histograms were automatically calculated after gating the desired population to exclude dead cells. PPIX was excited using 488 nm and emission was detected at 620 nm while Ce6 was excited at 633 nm and emission was detected at 660 nm (Abdel Gaber et al. 2018). To study the effect of FCS concentration, Sk-Br-3, MCF-7, U87, and HF-5 cells were

incubated for 4 h with either Ce6 concentration series (0.1–100 μM) or 5-ALA concentration series (0.075–4.8 mM). The incubation medium was either FCS-free or supplied with 10% FCS or 2% FCS. To study the effect of the incubation period, U87 cells were incubated with either Ce6 series (1–100 μM) for 15 min to 24 h or with 5-ALA concentration series (0.075 to 4.8 mM) for 1 or 8 h. To study the effect of Ce6 conjugate on Ce6 cellular uptake, Sk-Br-3, and HF-5 cells were incubated for 4 h in a medium supplied with 2% FCS with 5 μM Ce6 of either free Ce6 or MSN-Ce6.

Cellular localization assessment

Sk-Br-3 cells were incubated with either 10 μM Ce6 or 1.2 mM 5-ALA. U87 cells and spheroids were incubated with 5 μM Ce6 in the form MSN-Ce6 and free Ce6, respectively. All incubations were for 4 h in a medium supplied with 2% FCS. Nuclei were stained with Hoechst 33258 (Invitrogen, USA) as instructed by the manufacturer. Fluorescence was examined by Leica DM5000B fluorescent microscope (Leica, Germany).

Spheroid formation

Spheroids are 3-dimensional cellular structures characterized by a decreased gradient of oxygen and nutrient from the periphery to the center, similar to what is expected in an in vivo tumor mass (Pinto et al. 2020). Sk-Br-3, MCF-7, and U87 cells were cultured in FCS-free DMEM F-12 medium supplied with B27, basic fibroblast growth factor, and epidermal growth factor. Cells were cultured in ultra-low attachment T-flasks and left for 7 days in the incubator with minimal shaking (Abdel Gaber et al. 2018). To evaluate the growth kinetics, on the third day of culture, 3 spheres were transferred from the T-flasks to ultra-low attachment 96-well plates and they were imaged every 2 days for 2 weeks using the bright field of Leica DM5000B fluorescent microscope (Leica, Germany) at 10x magnification. The projected surface area of the formed spheres was estimated using Image J software downloaded from (www.NIH.org). Results were expressed as a fold increase in the projected area to the projected area of the respective spheres on the third day of culture.

Assessment of PDT efficiency

A group of dark control was included in which incubation with the highest tested PS concentration took place without irradiation. A group of laser control was included in which irradiation took place at the highest tested irradiation dose without prior PS incubation. A control group was included in which cells were neither incubated with PS nor irradiated.

For Ce6-PDT, Sk-Br-3, MCF-7, U87, and HF-5 cells were incubated for 4 h with either 5 or 10 μM Ce6 supplied in a 2% FCS-containing medium. For 5-ALA-PDT, Sk-Br-3, MCF-7, U87, and HF-5 cells were incubated with either 0.15 or 0.6 mM 5-ALA. For illumination, the PS-containing medium was removed and replaced with a phenol-red-free medium. Ce6 irradiation was conducted using a 665-nm diode laser (100 mW/cm^2) and 5-ALA irradiation was conducted using a 635 nm diode laser (100 mW/cm^2). The irradiation time varied to have an irradiation dose from 0.5 to 8 J/cm^2. Cells were cultured for another 4 h, and viability was measured using Cell titer blue assay (CTB) as previously

described (Kammerer et al. 2011). Results were expressed as viability % relative to the control. Conditions needed to kill 50% of the cell population (IC50) were estimated with a 95% confidence interval (El-Gogary et al. 2019).

For spheroid Ce6-PDT, U87 spheroids were incubated with 10 μM Ce6 for 4 h. Ce6 was removed, and spheroids were irradiated with 2.4 J/cm^2. A fresh medium was placed, and spheroids were imaged to monitor their projected surface area for 5 days after treatment. Results were expressed as the projected surface area of spheroids over time.

For Ce6 conjugate-PDT, Sk-Br-3, and HF-5 cells were incubated for 4 h in a medium supplied with 2% FCS with 5 μM Ce6 of either free Ce6 or MSN-Ce6. The Ce6-containing medium was removed and cells were irradiated with an irradiation dose of up to 8 J/cm^2. Cells were cultured for a further 4 h and viability was measured by CTB assay. Results were expressed as viability % relative to the controls.

Measurement of reactive oxygen species (ROS) production

ROS was measured using the 2′, 7′–dichlorodihydrofluorescein diacetate (DCFDA) kit (Abcam, Germany). Sk-Br-3, MCF-7, U87, and HF-5 cells were treated with IC50 conditions of 10 μM free Ce6-PDT. Before illumination by 45 min, cells were incubated with 25 μM of the supplied working solution. Directly after irradiation, the fluorescence was measured (Ex: 495 nm and Em: 522 nm) using a microplate reader (BMG LABTECH, Germany). Results were expressed as fold differences relative to the control (El-Gogary et al. 2019).

Assessment of cell death mode and caspase 3/7 level

Sk-Br-3, HF-5, and U87 cells were treated with IC50 conditions of 10 μM free Ce6-PDT or 0.6 mM 5-ALA-PDT. Cells were collected and stained with Annexin V FITC and propidium iodide following the manufacturer´s instructions (BD Pharmingen FITC Annexin V apoptosis detection kit) for 15 min at room temperature. Fluorescence was quantified using flow cytometry. Annexin V (green color; Ex = 488 nm, Em = 500–550 nm) and propidium iodide (red color; Ex = 514 nm, Em = 650–730 nm) (El-Gogary et al. 2019). For the caspase 3/7 quantification assay, Sk-Br-3, MCF-7, U87, and HF-5 cells were treated with IC50 conditions of 10 μM free Ce6-PDT or 0.6 mM 5-ALA-PDT. At the end of the 4-h post-irradiation period, cells were incubated for 1 h at room temperature with the caspase 3/7 substrate provided in the kit (Apo-ONE Homogenous Caspase 3/7 Assay, Promega). The fluorescence of the produced rhodamine 110 was measured (Excitation at 495 nm and emission at 522 nm). Caspase 3/7 activity was expressed as fold elevation compared to the control untreated group (El-Gogary et al. 2019).

Breast cancer rat model

The study was approved by the institutional animal care and use committee of Kafrelsheikh University. Adult female Wister rats (weight 100–150 g) were purchased from the Medical Experimental Research Center of Tanta University. Rats were acclimatized for 15 days with free access to food and water. The light cycle of 12 h darkness was maintained. For breast cancer induction, rats were administered 7,12-dimethylbenz(a)

anthracene (DMBA) dissolved in sesame oil as a single oral dose (20 mg/kg). Treatment was conducted 14 weeks after DMBA administration (Barros et al. 2004).

Treatment groups

Rats were grouped into five groups ($n=4$) as listed in Table 1. The biosafety and biodegradation of MSN were reported before (Mamaeva et al. 2011) and thus a group of "MSN only" was not included to minimize the number of used rats. Free Ce6 and MSN-Ce6 were intratumorally injected. For the PDT groups, irradiation with 180 J/cm^2 from a non-thermal LED source (660 nm, 100 mW/cm^2, 30 min) was conducted 24 h after Ce6 administration either in the free or the conjugate form. Rats were weighed and euthanized by cervical dislocation 2 weeks after applying PDT. Tissues were collected, and their weight and volume were recorded (Jeong et al. 2011). Volume was calculated using Eq. (3):

$$\text{Tumor volume} = \text{width}^2 \times \text{length} \times 0.5 \tag{3}$$

Histopathological assessment

Tissues were thoroughly washed with saline. They were fixed in paraformaldehyde and gradual dehydration protocol using elevating ethanol concentration (70–100%) was applied. They were embedded in paraffin and sliced into a 5-µm-thick section mounted on glass slides. Sections were stained using hematoxylin and eosin (Hematoxylin and Eosin Stain Kit, Vector Laboratories, CA, USA). Slides were examined using 40 × magnification of a light microscope where signs of inflammation, necrosis, and fibrosis were investigated (Abdel Khalek et al. 2021).

Immunohistochemical assessment

Deparaffinated sections were incubated overnight at 4 °C with 1:50 dilutions of rabbit-anti-cleaved caspase 3 or Bax antibodies (Cell Signaling Technology, USA). Sections were then incubated with biotinylated goat-anti-rabbit-IgG and streptavidin/alkaline phosphatase complex at 1:200 dilution. Slides were counterstained with hematoxylin and examined by 40 × objective. The expression level of caspase 3 and Bax was reported as average optical density collected from random 200 points (Cabral et al. 2021).

Table 1 Treatment groups to assess Ce6-PDT either in the free form or conjugated as MSN-Ce6 in treating breast cancer

Group	DMBA (20 mg/kg)	Ce6 (5 mg/kg)	Irradiation (180 J/cm^2)
Healthy control	No	No	No
Untreated control	Yes	No	No
Dark control	Yes	Yes	No
Free Ce6-PDT	Yes	Yes	Yes
MSN-Ce6-PDT	Yes	Yes	Yes

Statistical analysis

At least, each experiment was repeated 3 times, and presented are the average and standard deviation. Statistical analysis was applied using GraphPad Instat software using ANOVA and Tukey post-test ($P < 0.05$). P value was depicted as * when it was less than 0.05, as ** when it was less than 0.01, and as *** when it was less than 0.001.

Results

Ce6 cellular uptake, and intracellular localization

Cellular uptake of Ce6 was studied in relation to serum concentration (Fig. 1a) and compared to 5-ALA-PPIX (Fig. 1b). Results depicted are for Sk-Br-3 cells incubated for 4 h with a series of concentrations of either PS. The lack of serum was associated with a significantly higher cellular fluorescence of both Ce6 and PPIX at all tested concentrations when compared to the respective values when the medium was supplied with 10% serum. The findings for all cell lines are summarized in (Additional File 1: Table 1) . As seen, the highest fold difference in measured PPIX fluorescence was 10.4 fold and it was detected when MCF-7 cells were incubated with 0.3 mM 5-ALA. In the case of Ce6, the highest fold difference was 34.6 times, and it was measured when Sk-Br-3 cells were incubated with 5 µM Ce6.

The kinetics of Ce6 cellular uptake was measured over 24 h using U87 cells while fixing the serum concentration to 2% (Fig. 1c). A concentration-dependent increase in the cellular uptake was observed at all tested incubation periods. Ce6 was detected in the cells after 15 min (Additional file 1: Fig. S1). For a given concentration, PPIX cellular fluorescence increased with the increase of the 5-ALA-incubation time but reached a plateau at both tested incubation periods (Fig. 1d).

The cellular accumulation was studied with respect to the cell type as well. Cellular uptake of 5 and 10 µM Ce6 after 4 h incubation supplied in 2% FCS with all tested 4 cell lines (Fig. 1e) showed that U87 had the highest accumulation level and Sk-Br-3 cells the lowest. It is worth noting that the non-cancerous cell line HF-5 used as a model for healthy cells showed a high level of Ce6 uptake that was not statistically different from the uptake by U87 and MCF-7 cells when the concentration was 5 µM and was indifferent from MCF-7 when the concentration was 10 µM.

The cellular accumulation of PPIX after 4 h incubation with 5-ALA in a 2% FCS-containing medium (Fig. 1f) revealed that at 0.3 mM 5-ALA, MCF-7 showed the lowest PPIX cellular accumulation of the tested cell lines. At 1.2 mM 5-ALA, both MCF-7 and Sk-Br-3 cells showed a statistically insignificant difference in PPIX accumulation, and the same was observed for U87 and HF-5 cells. As shown, the PPIX accumulation levels in the tested breast cancer cells were 2 times higher than the respective values for U87 and HF-5 cells. Importantly, the increase in 5-ALA concentration was not associated with an increase in the PPIX accumulation for U87 and HF-5.

The cellular localization of Ce6 was investigated by fluorescence microscopy after incubating Sk-Br-3 cells for 4 h with 10 µM Ce6 supplied in 2% FCS. As shown in Fig. 1g, this water-soluble form of Ce6 succeeded to permeate the cell membrane and was homogeneously distributed within the cytoplasm of the cells. This finding illustrated that the quantified fluorescence signal detected by flow cytometry was mainly originating from intracellular Ce6. The same cell line was incubated with 1.2 mM

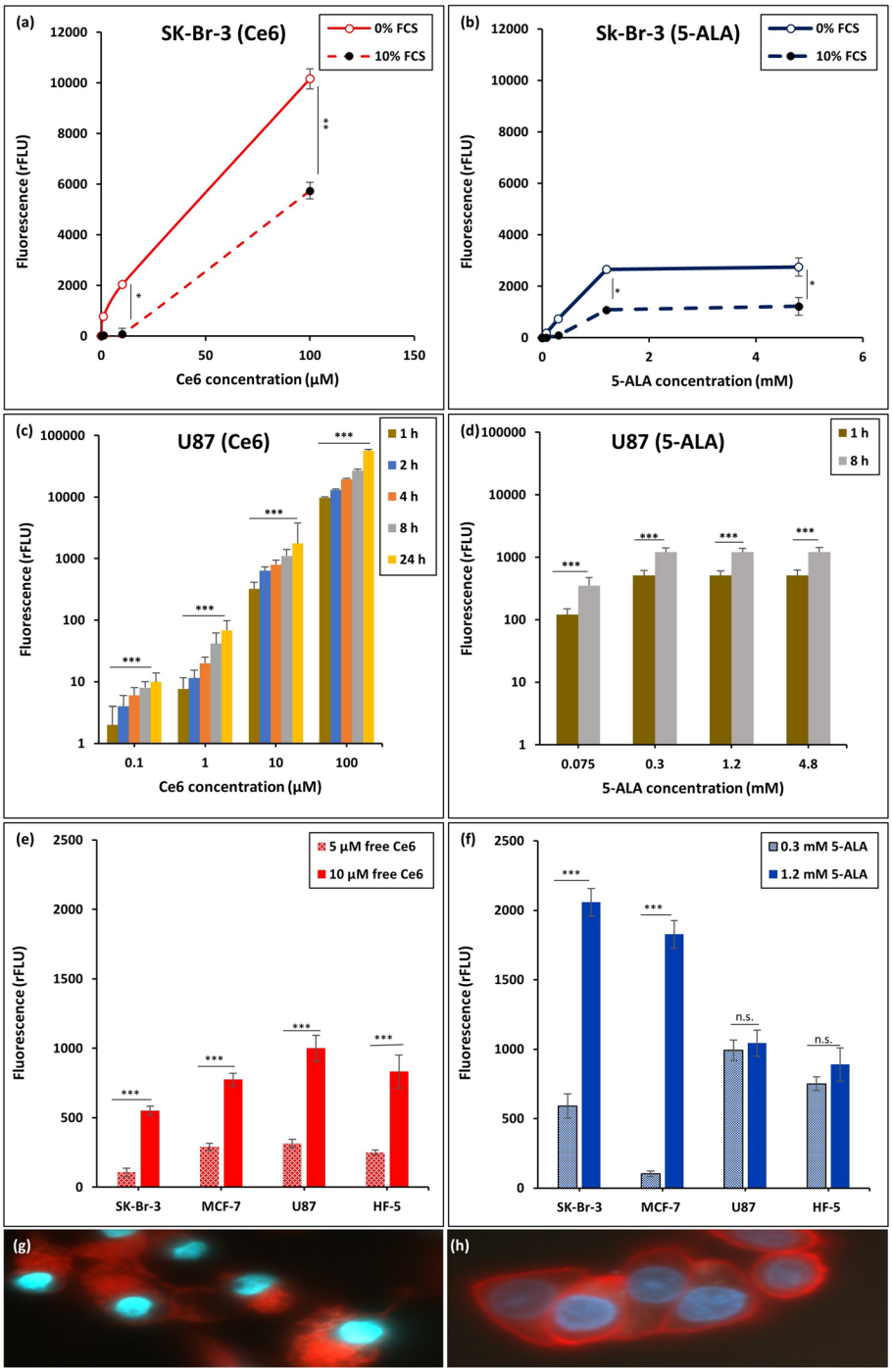

Fig. 1 **a** Cellular uptake of Sk-Br-3 cells incubated for 4 h with a series of Ce6 concentrations in the absence of fetal calf serum (FCS) and in the presence of 10% FCS. **b** Cellular uptake of Sk-Br-3 cells incubated for 4 h with a series of 5-ALA concentrations in the absence of FCS and in the presence of 10% FCS. **c** Cellular uptake of U87 cells incubated with a series of Ce6 concentrations for 1–24 h in the presence of 2% FCS. **d** Cellular uptake of U87 cells incubated with a series of 5-ALA concentrations for 1 and 8 h in the presence of 2% FCS. **e** Ce6 cellular accumulation in Sk-Br3, MCF-7, U87 and HF-5 cells after 4 h incubation with either 5 or 10 µM Ce6 in the presence of 2% FCS. **f** 5-ALA-PPIX cellular accumulation in Sk-Br3, MCF-7, U87 and HF-5 cells after 4 h incubation with either 0.3 or 1.2 mM 5-ALA in the presence of 2% FCS. **g** Representative fluorescence image of Sk-Br-3 incubated for 4 h with 10 µM Ce6 supplied in 2% FCS. **h** Representative fluorescence image of Sk-Br-3 cells incubated for 4 h with 1.2 mM 5-ALA supplied in 2% FCS

5-ALA for 4 h in 2% FCS-containing medium, and as seen in Fig. 1h, PPIX showed a distinct tendency to accumulate at the cell membrane.

In vitro Ce6-PDT

Based on the previous findings, an incubation period of 4 h in a medium supplied with 2% FCS was selected for the in vitro PDT evaluations. Ce6-PDT was conducted on all tested cell lines using either 5 or 10 µM Ce6, and irradiation doses up to 8 J/cm^2. The viability results of Sk-Br-3, MCF-7, U87, and HF-5 cells are presented in Fig. 2 a, c, e, and g, respectively. Neither the dark control in the presence of 10 µM Ce6 nor the irradiation of the cells at 8 J/cm^2 without Ce6 exerted any cytotoxicity on any of the tested cell lines.

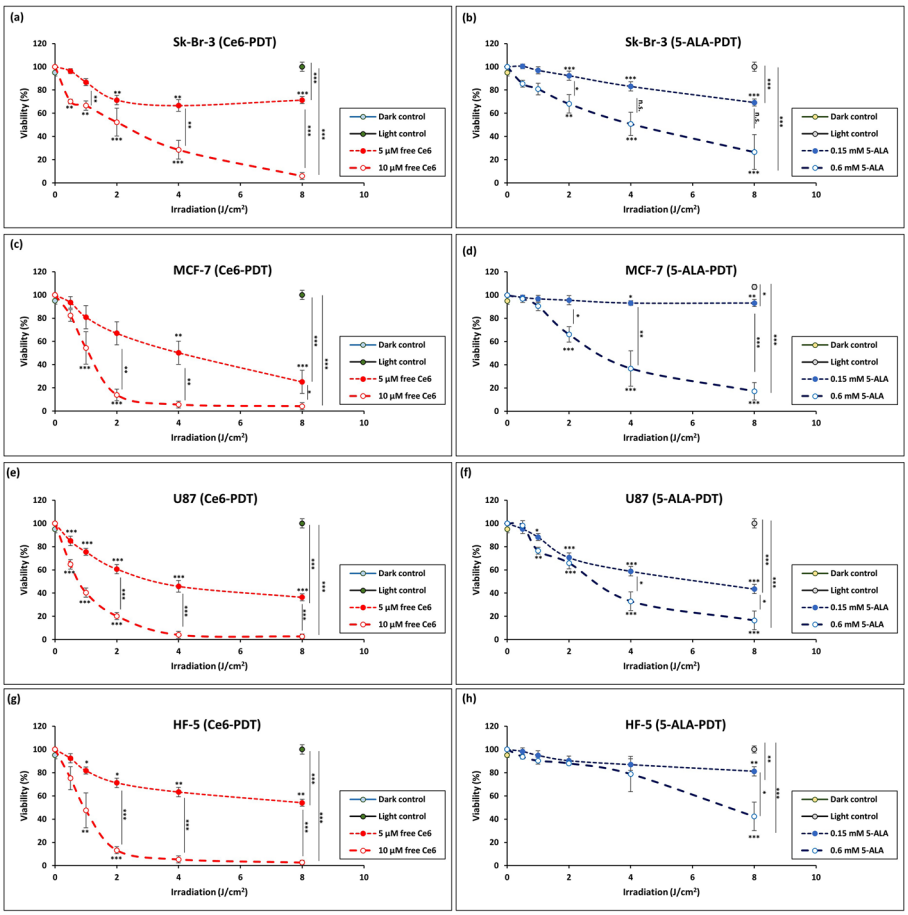

Fig. 2 **a** Sk-Br-3, **c** MCF-7, **e** U87, **g** HF-5 cells viability results after 4 h incubation with either 5 or 10 µM Ce6 followed by irradiation with 665 nm for various durations. In the dark control group, cells were incubated with 10 µM Ce6 for 4 h without irradiation, and in the light control group, cells were irradiated with 8 J/cm^2 without prior Ce6 incubation: **b** Sk-Br-3, **d** MCF-7, **f** U87, **h** HF-5 cells viability results after 4 h incubation with either 0.15 or 0.6 mM 5-ALA followed by irradiation using 635 nm. In the dark control group, cells were incubated with 0.6 mM 5-ALA for 4 h without irradiation and in the light control group, cells were irradiated with 8 J/cm^2 without prior 5-ALA incubation. Experiments were repeated at least 3 times and presented are mean and standard deviation

Table 2 Summary of conditions needed to reach IC50 of Sk-Br-3, MCF-7, U87, and HF-5 after Ce6-PDT and 5-ALA-PDT

Irradiation needed to reach IC50 (J/cm^2)					Irradiation needed to reach IC50 (J/cm^2)				
	Sk-Br-3	MCF-7	U87	HF-5		Sk-Br-3	MCF-7	U87	HF-5
5 µM Ce6	> 8	4	4	> 8	0.15 mM 5-ALA	> 8	> 8	7	> 8
10 µM Ce6	3.5	1	0.8	1	0.6 mM 5-ALA	4	3	3	8

There was a significant decline in the cell viability for a given Ce6 concentration with increasing irradiation dose. Moreover, there was a statistically significant, concentration-dependent decrease in viability at a given irradiation dose (Fig. 2 a, c, e, g). The cells varied in their responsiveness to Ce6-PDT, as summarized in Table 2. At 5 µM Ce6, HF-5, and Sk-Br-3 were the least responsive cell lines and did not reach 50% cell death (IC50) within the tested irradiation dose range. At a Ce6 concentration of 10 µM, there was a 4 -times decrease in the irradiation dose needed to reach IC50 for both MCF-7 and U87 cells. The breast cancer cell line Sk-Br-3 required a 3.6 times higher irradiation dose than the other three cell lines (HF-5, U87, and MCF-7) to reach IC50.

For comparison, the 4 cell lines were treated with 0.15 and 0.6 mM 5-ALA-PDT at 4 h incubation in a medium supplied with 2% FCS and with an irradiation dose of up to 8 J/cm^2. The results are shown in Fig. 2b, d, f, and h, respectively. As for Ce6, the control experiments showed no cytotoxicity. As summarized in Table 2, at 0.15 mM 5-ALA, none of the cell lines reached IC50 except U87 cells, which reached IC50 at an irradiation dose of 7 J/cm^2. When the concentration was 0.6 mM 5-ALA, the most responsive cell line was Sk-Br-3 as it required only 3 J/cm^2 to reach IC50, while both U87 and MCF-7 required 4 J/cm^2. The least responsive cell line was HF-5, in line with the known selectivity of 5-ALA towards cancer cells.

In vitro, Ce6-PDT triggered ROS production and mode of cell death

ROS produced in the different cell lines were measured directly after PDT (10 µM Ce6-PDT, varying irradiation dose) and the results are presented in Fig. 3a. A significant increase in the ROS levels as compared to the control was observed in all cell lines. At all irradiation doses, U87 cells were the highest ROS-producing cells, while Sk-Br-3 and HF-5 cells were the lowest ROS-producing ones.

Irradiation doses corresponding to IC50 at 10 µM Ce6-PDT were applied to the different cell lines, and the mode of cell death was investigated (Fig. 3b). Cells exhibited both apoptotic and necrotic cell death modes. On the contrary, corresponding measurements using 0.6 mM 5-ALA-PDT showed a predominant apoptotic cell death mode (Fig. 3c). The observed apoptotic death mode was caspase-dependent for both Ce6 (Fig. 3d) and 5-ALA-PDT (Fig. 3e), as evidenced by the significant elevation in the caspase 3/7 level exemplifying the executioner caspases in all tested cell lines compared to the control. SK-Br-3 showed the lowest level of caspase 3/7 following Ce6-PDT which matched having the lowest percentage of apoptotic cells observed for this cell line.

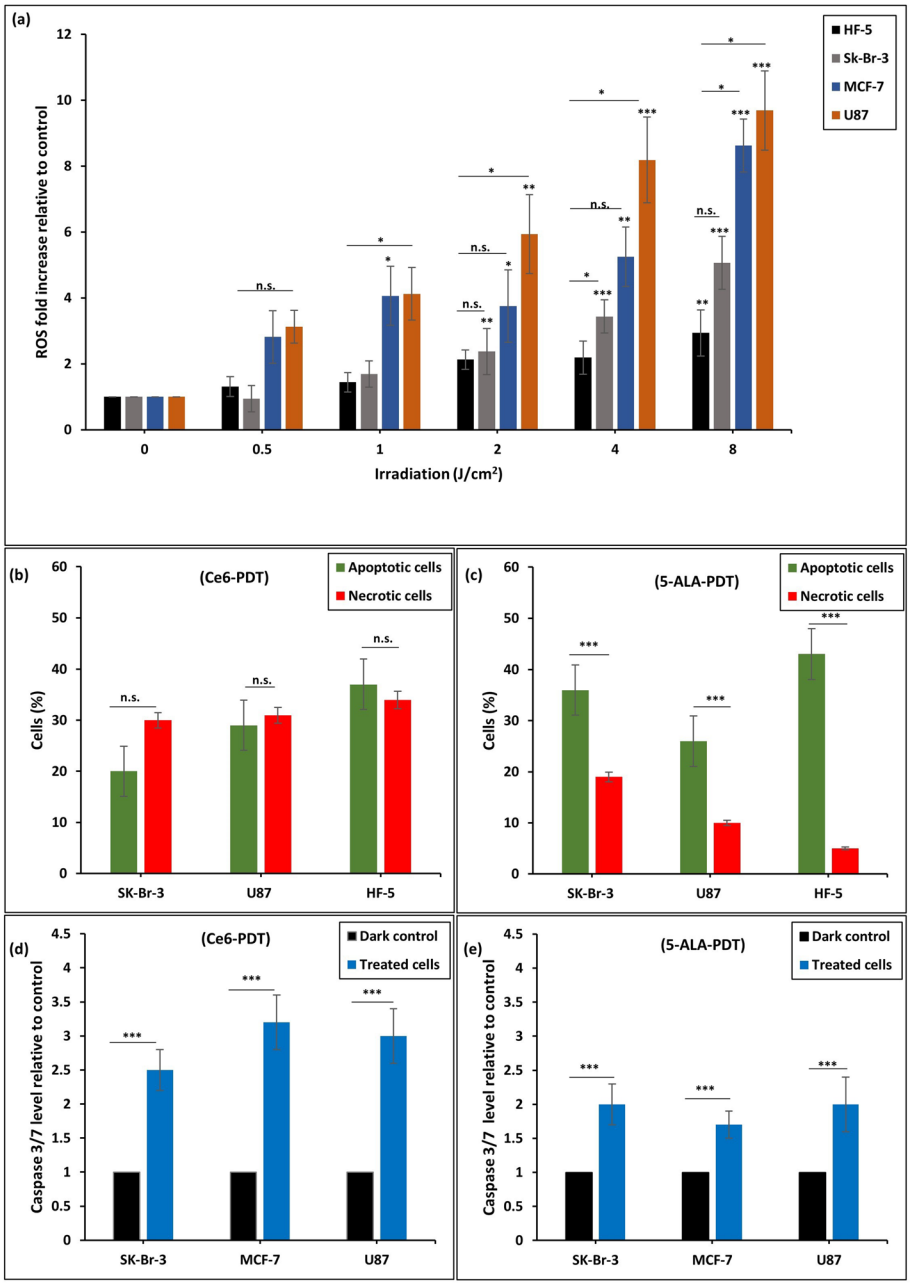

Fig. 3 **a** ROS production level of Sk-Br3, MCF-7, U87, and HF-5 after 4 h incubation with 10 μM Ce6 followed by irradiation using 665 nm for various durations expressed as fold difference relative to the control. **b** Apoptotic and necrotic % of Sk-Br-3, U87, and HF-5 cells after treatment with 10 μM Ce6-PDT conditions corresponding to IC50 conditions. **c** Apoptotic and necrotic % of Sk-Br-3, U87, and HF-5 cells after treatment with 0.6 mM 5-ALA-PDT conditions corresponding to IC50 conditions. **d** Caspase 3/7 level of Sk-Br-3, MCF-7, and U87 cells after treatment with 10 μM Ce6-PDT conditions corresponding to IC50 conditions. **e** Caspase 3/7 level of Sk-Br-3, MCF-7, and U87 cells after treatment with 0.6 mM 5-ALA-PDT conditions corresponding to IC50 conditions. Treatment conditions are summarized in Table 3. All experiments were repeated at least 3 times and presented are mean and standard deviation

Glioma spheroids Ce6-PDT

Sk-Br-3 and MCF-7 cells formed irregular spheroids, and tended to form bulky spheroid clusters, while U87 cells produced regularly spherical shaped ones (Additional

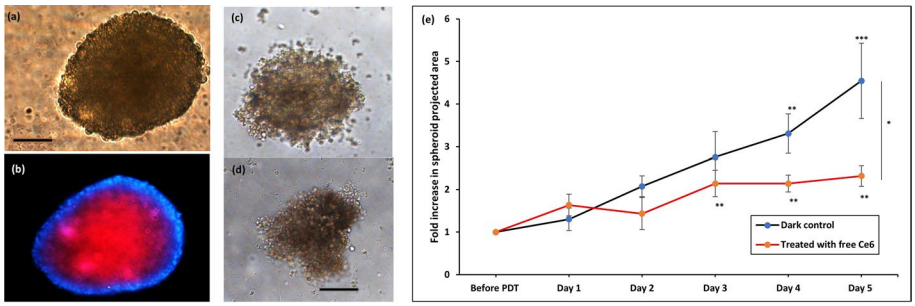

Fig. 4 **a** Representative image of U87 spheroid using a light microscope. **b** Representative image of U87 spheroid using fluorescence microscope after incubation for 4 h with 10 µM Ce6 and staining the nuclei with Hoechst 33258. **c** Representative light microscope image of U87 spheroid treated with Ce6-PDT on day 0. **d** Representative light microscope image of U87 spheroid treated with Ce6-PDT on day 3. **e** Fold increase of U87 spheroid projected area monitored over 5 days after incubation for 4 h with 10 µM Ce6 followed by 2.4 J/cm^2 irradiation using 665 nm compared to the dark control group in which spheroids were only incubated with 10 µM Ce6 without irradiation. Spheroids were imaged using 10 × magnification. Experiments were repeated at least 3 times and presented are mean and standard deviation

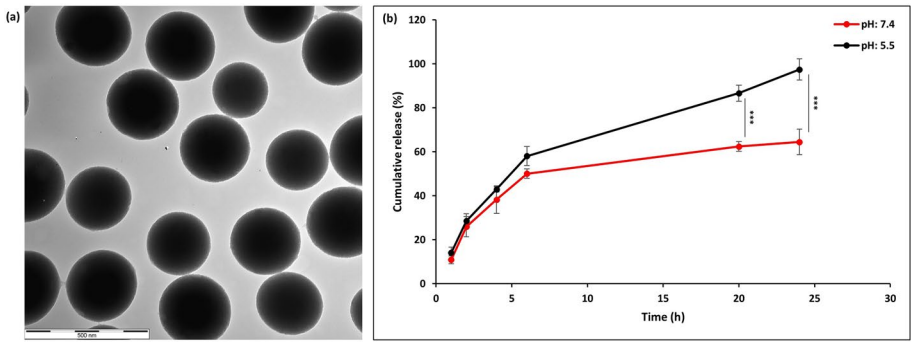

Fig. 5 **a** Transmission electron microscope image of amine-functionalized mesoporous silica nanoparticles. **b** Ce6 release profile of MSN-Ce6 conjugate sonicated in phosphate buffer saline at room temperature in pH: 5.5 or pH: 7.5 over 24 h

file 1: Fig. S2). Thus, U87 spheroids were selected for further studies. Incubating U87 spheroids (Fig. 4a) with Ce6 resulted in an evident fluorescence, confirming Ce6 cellular uptake (Fig. 4b). Upon illumination, the periphery of the spheroids became loose, and cell dissociation progressed with time (Fig. 4c, d). Incubation of the spheroids without illumination (dark control group) resulted in a 5 times increase in the spheroid projected surface area on the fifth day of treatment. One session of Ce6-PDT suppressed the growth, resulted in a significant decline in the projected area by 60% (Fig. 4e) and the corresponding volume by 75% at day 5 after PDT compared to dark control spheroids.

MSN-Ce6-conjugate characterization and release

As the PDT efficiency of Ce6 was evidently directly correlated with the extent of cellular uptake, we hypothesized formulating Ce6 together with cationic MSN would lead to higher apoptosis levels for Sk-Br-3 cells. We, therefore, synthesized highly amino silane-functionalized MSN through co-condensation, resulting in particles having an amino silane content of 16.5 wt%, a particle diameter of 313 ± 21 nm (Fig. 5a), an average pore size of 5 nm, and a specific surface area of 915 m^2/g. The zeta-potential value measured

in 1 mM KCl was + 28 m, in agreement with the high amino silane content. Ce6 was then covalently linked to the particles using EDC/NHS coupling, and the coupling efficiency was 99.9% resulting in a Ce6 content of 20% wt/wt.

FT-IR spectroscopy (Additional file 1: Fig. S3) confirmed a successful covalent Ce6 conjugation to the MSN, as a band appeared at 1636 cm^{-1} after conjugation, which could be assigned to an amide carbonyl bond (Aboelmaati et al. 2021). Ce6 release from MSN-Ce6 conjugate was quantified spectrophotometrically over 24 h either in pH of 7.4 or pH 5.5 buffers, to mimic the pH-conditions in the bloodstream and the tumor stroma acidic environment (Fig. 5b). At both pHs, 40% of Ce6 was released within the first 6 h, while the corresponding values measured after a release time of 24 h was 97% at pH = 5.5 and 65% at pH = 7.4.

MSN-Ce6 cellular uptake, localization, and PDT

The cellular uptake of MSN-Ce6 by Sk-Br-3 cells was determined by FACS. The use of the MSN-Ce6 conjugate significantly increased Ce6 cellular uptake as compared to free Ce6, as shown in Fig. 6a. For example, at a Ce6 concentration of 5 μM, internalized Ce6 was sevenfold to that of free Ce6. At higher concentrations, the uptake of Ce6 was also clearly enhanced when conjugated to MSN, but the relative difference in uptake when compared to free Ce6 decreased with increasing Ce6 concentration and was about threefold at a Ce6 concentration of 10 μM. The increased Ce6 uptake was also reflected in the PDT efficiency, as shown in Fig. 6b. The viability of the Sk-Br-3 cells irradiated once for 40–80 s with an intensity in the range of 4–8 J/cm^2 decreased from about 75% in case of free Ce6 to less than 20% in the case of MSN-Ce6-PDT. Ce6 administered using the MSN-Ce6 conjugate was mainly localized in the cytoplasm of U87 cells that had been incubated for 4 h with 5 μM Ce6 concentration (Fig. 6c). The distribution closely resembled that of free Ce6 (Fig. 1g).

Similar findings were seen in HF-5 cells (Fig. 6d). We note that the high PDT efficiency was also seen for the non-cancer cell line HF-5 (Fig. 6e).

In vivo PDT response

Inspired by the promising in vitro results obtained by the Ce6-MSN conjugate, we pursued an in vivo study focusing on a very aggressive type of breast cancer chemically induced by the administration of the immunosuppressor DMBA to rats. Based on the low in vitro selectivity of the Ce6-MSN particles, intratumoral administration was used, and the results were compared with corresponding results obtained for free Ce6. Either free Ce6 or MSN-Ce6 was injected, followed by 30 min irradiation using a non-thermal LED (100 mW/cm^2) 24 h after Ce6 administration. Images of the tumors collected at the end of the experiments, i.e., 2 weeks after a single PDT application, showed a visually evident treatment success in the case of both MSN-Ce6 and free Ce6 groups compared to the dark control or the untreated control groups (Fig. 7a). The reduction in the tumor volume compared to the untreated control was 30% in the case of free Ce6-PDT and 50% in the case of Ce6-MSN-PDT (Fig. 7b). A significant decline in the collected tumor mass was also observed; 1.6 ± 0.13 g in the case of the untreated control, 1.12 ± 0.12 g in the case of free Ce6-PDT (30% reduction), and 0.67 ± 0.09 g in the case of MSN-Ce6-PDT

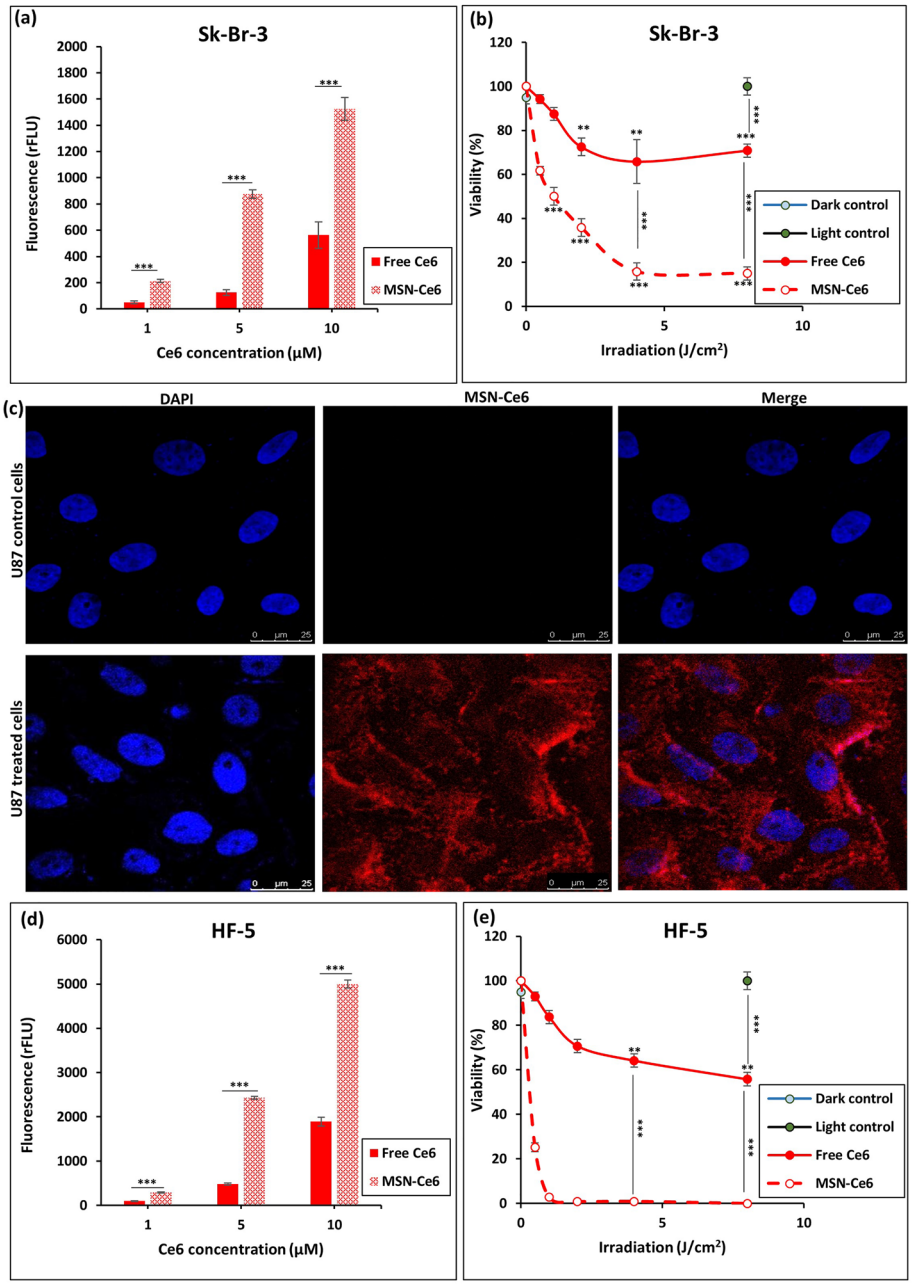

Fig. 6 **a** Cellular uptake of Sk-Br-3 after 4 h incubation with either 5 μM free Ce6 or the same concentration of Ce6 but in the MSN-Ce6 conjugate form. **b** Viability results of Sk-Br-3 cells incubated for 4 h with 5 μM free Ce6 or the same concentration of Ce6, but in the MSN-Ce6 conjugate form followed by irradiation using 665 nm for various durations. **c** Representative fluorescence images of U87 control cells and cells incubated for 4 h with 5 μM Ce6 in the MSN-Ce6 conjugate form showing the nuclei stained with Hoechst 33258, Ce6 fluorescence and the merge of both. **d** Cellular uptake of HF-5 after 4 h incubation with either 5 μM free Ce6 or same concentration of Ce6 but in the MSN-Ce6 conjugate form. **e** Viability results of HF-5 cells incubated for 4 h with 5 μM free Ce6 or the same concentration of Ce6, but in the MSN-Ce6 conjugate form followed by irradiation using 665 nm for various durations. Experiments were repeated at least 3 times and presented are mean and standard deviation

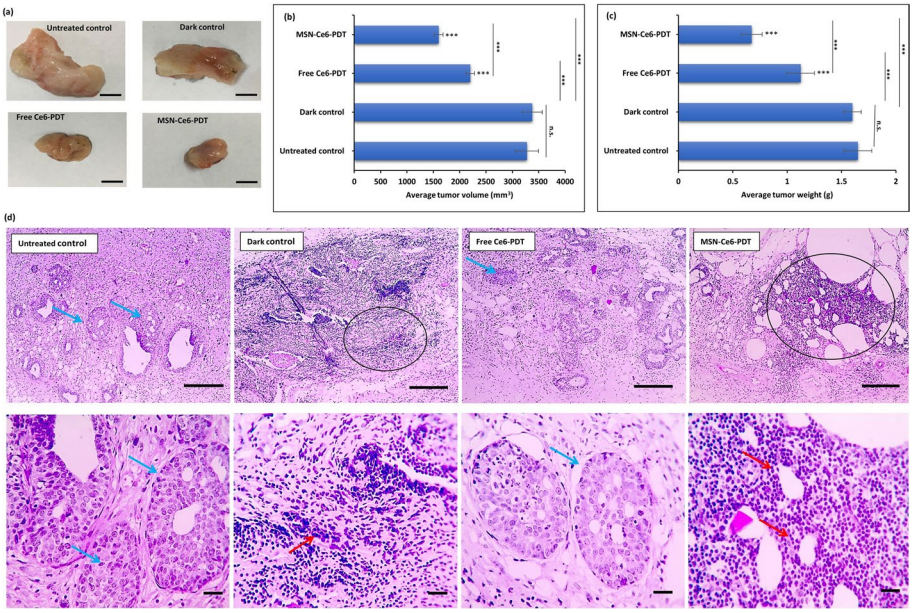

Fig. 7 **a** Representative photo images of collected tumor tissues of DMBA-induced breast cancer rats from the untreated group, dark control group (administered 5 mg/kg Ce6 with no irradiation), free Ce6-PDT group (administered 5 mg/kg of free Ce6 followed by 180 J/cm^2 irradiation using 665 nm) and MSN-Ce6-PDT group (administered dose equivalent to 5 mg/kg of Ce6 followed by 180 J/cm^2 irradiation using 665 nm) bar 9 mm. **b** Average tumor volume. **c** Average tumor weight. **d** Histopathological images of hematoxylin and eosin stained non-lactating mammary gland tissues collected from the aforementioned treatment groups. Blue arrows marked the lumen of the duct filled with atypical proliferative cells and red arrows marked the malignant epithelial cells invading the stroma forming small ductal structures (upper row X:100 bar 100 µm, lower row X: 400 bar 50 µm)

(60% reduction) (Fig. 7c). Those findings showed that the observed enhancement of PDT response in vitro (Fig. 6b) was valid also in vivo.

Histological examination of collected tissues (Fig. 7d) revealed that a very invasive ductal carcinoma in situ (DCI) was developed in the untreated control, where the epithelial cells filled and expanded the ducts forming glandular spaces. Necrotic and dysplastic ducts were surrounded by necrotic and inflamed stroma mainly due to neutrophil infiltration that caused extensive comedo necrosis (blue arrows). A similar histological picture was seen in the case of the dark control group where malignant epithelial cells invading the stroma forming small ductal structures (red arrows), and large areas of necrosis with the infiltration of some inflammatory cells were seen. The severity of the DCI decreased in the free Ce6-PDT group and was the mildest in the case of the MSN-Ce6-PDT group.

In vivo MSN-Ce6-PDT relation with caspase 3 and Bax levels

The expression of caspase 3 (Fig. 8a) and Bax (Fig. 8b) in the tissues of dark control, free Ce6 (5 mg/kg) and MSN-Ce6 (5 mg/kg) were studied by immunohistochemical assays. As demonstrated in the optical density percentage of caspase 3 (Additional file 1: Fig. S4) and Bax staining (Additional file 1: Fig. S5), the expression of both caspase 3 and Bax was significantly elevated in the treated groups compared with the dark control and were significantly higher in the case of MSN-Ce6-PDT compared to the group of Ce6-PDT.

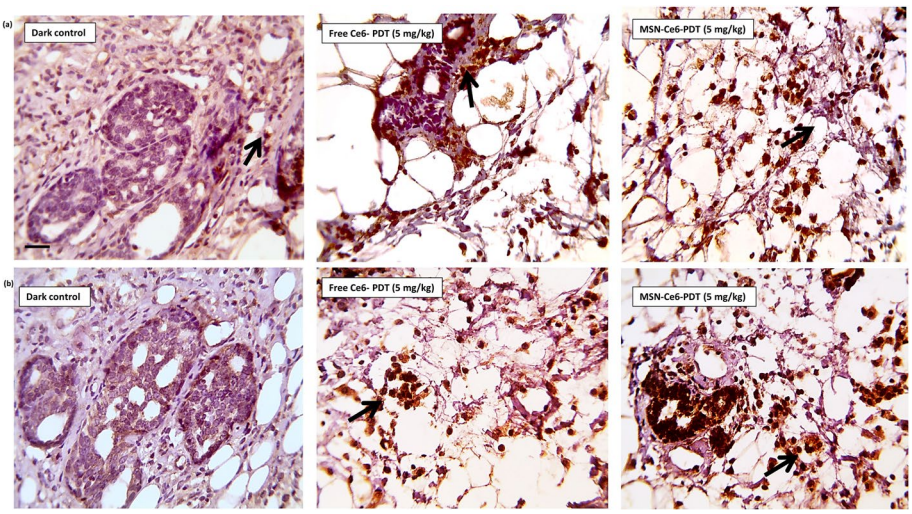

Fig. 8 **a** Microscopic images of immunostained breast sections against caspase 3 counterstained with Mayer's hematoxylin showing positively stained infiltrating tumor cells (black arrows) around affected lactating duct. **b** Microscopic images of immunostained breast sections against Bax counterstained with Mayer's hematoxylin showing positively stained infiltrating tumor cells (black arrows) around the affected lactating duct. The dark control group was DMBA-induced breast cancer rats administered 5 mg/kg Ce6 with no irradiation, the free Ce6-PDT group was DMBA-induced breast cancer rats administered 5 mg/kg of free Ce6 followed by 180 J/cm^2 irradiation using 665 nm and MSN-Ce6-PDT group was DMBA-induced breast cancer rats administered dose equivalent to 5 mg/kg of Ce6 followed by 180 J/cm^2 irradiation using 665 nm (X: 400 bar 50 µm)

Discussion

The anticancer PDT efficiency of a water-soluble form of Ce6 was investigated. Its cellular uptake was greatly reduced in the presence of serum proteins as compared to the benchmark used in this study, 5-ALA-PPIX (Table 1 in supplementary material). This could indicate that trisodium salt of Ce6 is adsorbed to serum proteins, which in turn can reduce cellular uptake. From a translational point of view, such adsorption could be attractive (Jeong et al. 2011), but the formation of Ce6–protein complexes remains speculative at this stage. Those findings were in agreement with a previous study using Sn(IV) chlorine e6 dichloride trisodium salt, (Al-Khaza'leh et al. 2011). The major protein components of serum are albumin and low-density lipoproteins (LDL). It was reported that Ce6 (acid form) binds to both types of proteins, with an association constant to albumin of $1.8 \pm 0.2 \times 10^8$ M^{-1} and $6.9 \pm 1.0 \times 10^7$ M^{-1} for LDL. The complexation was found to be pH dependent, increased for LDL and decreased for albumin (Mojzisova et al. 2007a) at lower pH values. It is a desirable feature that the PS is carried in the bloodstream by abundantly present proteins such as albumin. For the delivery to acidic tumor stroma, it is of particular interest that the binding constant is lowered at acidic pH to allow for the detachment of the PS from the protein carrier.

Ce6 was intracellularly detected after 15 min (Additional file 1: Fig. S1) which is in line with previous reports that could detect Ce6 in human fibroblasts 15 min after incubation (Mojzisova et al. 2007b). In a previous study, this form of Ce6 was used for PDT application against multidrug-resistant *Staphylococcus aureus* after 30 min of incubation (Winkler et al. 2016). The demonstrated fast cellular uptake and concentration-dependent

increase in the fluorescence signal (Fig. 1c) implied the potential suitability of the used trisodium salt of Ce6 for outpatient time-sparing diagnosis sessions. In the case of 5-ALA, the increase in concentration and incubation period resulted in a plateau of accumulated PPIX (Fig. 1d). This plateau can be explained by the need for the enzymatic conversion of 5-ALA into PPIX which takes place in the mitochondria. The availability of the enzyme ferrochelatase is negatively affecting the accumulation of PPIX as confirmed by the significant increase in the accumulated PPIX upon administration of ferrochelatase inhibitors (Fukuhara et al. 2013; Teng et al. 2011).

Representative human cell lines of glioblastoma (U87) and breast cancer (Sk-Br-3 and MCF-7) in addition to normal skin fibroblasts (HF-5) were studied for their ability to accumulate Ce6 after 4 h of incubation and their corresponding phototoxic activity was studied. Phototoxicity results (Table 2) were in line with the cellular accumulation findings (Fig. 1e) and indicated that Sk-Br-3 was the least responsive cell line to Ce6-PDT. We hypothesized that a nanosystem capable of increasing the cellular uptake of Ce6 would overcome the observed Sk-Br-3 resistance to Ce6-PDT. Cationic nanoparticles were selected since they have repeatedly been shown to be internalized more efficiently by cancer cells as compared to anionic nanoparticles (Heuts et al. 2021; Jambhrunkar et al. 2014; Lin et al. 2019; Panariti et al. 2012), and lead to enhanced therapeutic outcomes (Wang et al. 2016; Wittig et al. 2013). Furthermore, the large surface area and pore volume of MSN should allow for high Ce6 loading.

The use of cationic MSN as carriers for Ce6 led to a higher accumulation of Ce6 in the Sk-Br-3 cells (Fig. 6a), for which otherwise a low cellular uptake and/or high efflux was observed, and the higher intracellular Ce6 concentrations achievable with MSN led to a pronounced increase in the PDT activity (Fig. 6b) (an up to sevenfold increase in cellular uptake as compared to free Ce6, and a tenfold increase in therapeutic response in vitro). This finding suggested that the poor internalization of free Ce6 by the Sk-Br-3 cells indeed was the main reason for the poor PDT efficiency of free Ce6 in this case. An efficient endosomal escape of Ce6 from the MSN preferentially residing in endosomes and lysosomes was confirmed by the observed cytoplasm localization of Ce6 after MSN-Ce6 administration (Fig. 6c).

The higher PDT activity achieved with MSN-Ce6 as compared to that of free Ce6 was also mirrored in vivo in a model for aggressive breast cancer. Compared to the allograft model developed by murine cell inoculation, the DMBA model, particularly when using rats instead of mice, is considered more aggressive and challenging to treat (Zeng et al. 2020). Here, a 1.7-fold increase in therapeutic outcome was observed for the intratumorally injected MSN-Ce6 as compared to free Ce6 (Fig. 7b) and correlated with an increase in caspase 3 expression (Fig. 8a). Those results are consistent with the obtained caspase-dependent (Fig. 3d) apoptotic death mode (Fig. 3b) in vitro findings and agreed with the elevation of caspase 3 and Bax levels reported for Ce6-PDT of osteosarcoma (Yu et al. 2020). Necrosis was also reported in our case which differed from the reported purely apoptotic cell death modes for the acidic form of Ce6 (Wawrzyńska et al. 2010), Ce6 polyvinyl pyrrolidone complex (Ali-Seyed et al. 2011; Chin et al. 2008) or Ce6-C-15-ethyl ester (Wang et al. 2022). One possible explanation for the observed necrotic cell death mode is a shift from an excessive apoptotic mode (Nicotera and Melino 2004).

The synthesized MSN-Ce6 showed a loading efficiency of 20% which is high in comparison to most literature reports on comparable systems (Table 2 in Additional file 1), and just slightly lower than the highest Ce6 loading degree reported in the literature, 22 wt%. The latter was obtained through the physisorption of acidic Ce6 to dendritic MSN from water (Xu et al. 2019). However, the latter case had a lower encapsulation efficiency. In our system, almost 40% of Ce6 was released in the first 4 h (Fig. 5b). The fast-release kinetics can be related to a detachment of aminosilanes from the silica network, in combination with the hydrolysis of the silica network, a process that can be catalyzed by the presence of basic amino-functions (Etienne and Walcarius 2003). The fast particle dissolution can also be connected to the fact that the silica network in co-condensed MSN has a lower degree of condensation than often used calcined MSN, and the degree of silica condensation is directly reflected in the dissolution kinetics (Möller and Bein 2019). However, we note that the silica dissolution-triggered release of Ce6 will probably be slightly lower in the presence of serum proteins (Lin et al. 2022), but the results highlight the suitability of the MSN as carriers for Ce6.

Our synthesized MSN-Ce6 significantly enhanced the therapeutic response of free Ce6 more than many reported nanosystems such as (Kim et al. (2020), Song et al. (2022) and Su et al. (2017) (Table 2 in Additional file 1) as indicated by the significantly mild conditions needed to reach IC50 at the in vitro level (lowest reported irradiation of 0.88 J/cm^2, among the shortest incubation periods of only 4 h and the lowest concentrations of only 5 μM). As listed, some nanosystems were less phototoxic than free Ce6 (Gaio et al. 2019; Lee et al. 2017) and others decreased cancer cell viabilities from 60 to 65% in the case of free Ce6 to 50% (Feng et al. 2019; Kumari et al. 2019; Xiao et al. 2012). Spheroids simulate allografts to a great extent (Pinto et al. 2020) and our hydrophilic Ce6 suppressed the spheroid volume by 75% compared to the control after one treatment session (Fig. 4e). Those findings are superior to an earlier study where higher fluence was applied (30 J/cm^2), but to reach only 50% reduction in spheroid radius %, 10 days post-PDT were required (Gaio et al. 2019). At the in vivo level, our study is the only one using aggressive DMBA-induced rats (Zeng et al. 2020) as a breast cancer animal model (Table 2 in Additional file 1). A humane endpoint of the experiment was after 15 days, and the measured control tumor volume reached 3200 mm^3 which clearly demonstrates the severity of the disease. Our synthesized MSN-Ce6 managed to suppress the tumor volume by 50% compared to the control. As listed, the obtained results are satisfying when compared to other nanosystems. It should be noted that the results of the used hydrophilic Ce6 were superior to the reported ones in which the hydrophobic form was used.

A low selectivity for cancer cells was observed for both free Ce6 (Table 2) and the MSN-Ce6 conjugate (Fig. 6d, e), although HF-5 cells produced the lowest ROS level after illumination (Fig. 3a). Molecular and biochemical reasons for differential cellular responses should be studied to fully understand the obtained results. Those findings suggest that further developments should be directed towards enhancing the uptake kinetics in the cancer cells by active targeting approaches.

Conclusion

This study has demonstrated the PDT efficiency of the water-soluble trisodium salt of Ce6 in treating breast and glioma cancers delineated by rapid cellular accumulation, ROS production upon illumination, and the induction of caspase-dependent apoptotic cell death mode in addition to a necrotic one. Conjugating Ce6 to MSN has significantly enhanced the cellular uptake and the PDT response of Ce6 at both the in vitro and the in vivo levels. Further developments should focus on improving the selectivity towards cancer cells.

Supplementary Information

The online version contains supplementary material available at https://doi.org/10.1186/s12645-023-00216-4.

Additional file 1. Fig. S1: Cellular uptake of Ce6 after 15 min incubation with U87 cells. **Fig. S2**: Representative spheroids of Sk-Br-3 (a), MCF-7 (b) and U87 cells (c). **Fig S3**: FTIR spectra of free Ce6, MSN and MSN-Ce6 conjugate. **Fig. S4**: Caspase3 average optical density of DMBA-induced breast cancer rat model treated with 5 mg/kg Ce6 in the dark control, free Ce6-PDT and MSN-Ce6-PDT groups. **Fig. S5**: Bax average optical density of DMBA-induced breast cancer rat model treated with 5 mg/kg Ce6 in the dark control, free Ce6-PDT and MSN-Ce6-PDT groups. Table (1): Cellular uptake of 5 and 10 µM Ce6, 0.3 and 1.2 mM 5-ALA incubated with Sk-Br-3, MCF-7, U87, and HF-5 cells for 4 h in either serum-free medium or medium supplied with 10% FCS. Table (2): Summary of our findings compared to relevant studies.

Acknowledgements

The contribution of the German Pharmaceutical Company Synverdis GmbH is acknowledged for providing the used hydrophilic Ce6 form. The Arab-German Young Academy of Sciences and Humanities (AGYA) is acknowledged for the support in study accomplishment. AGYA is funded by the German Federal Ministry of Education and Research (BMBF) grant 01DL20003. GUC-DAAD Bilateral Doctoral fellowship is acknowledged for the funded research stay of Sara A. Abdel Gaber at The Laser-Forschungslabor (LFL) at the LIFE-Center of the Hospital of the University of Munich.

Author contributions

SAAG conducted the investigation, formal analysis, methodology, writing original manuscript and participated in the conceptualization. Conceptualization, supervision, review, and editing were conducted by HS, MHAK and ML. All authors read and approved the final manuscript.

Funding

This study was partially funded by the Arab-German Young Academy of Sciences and Humanities (AGYA). AGYA draws on support from the German Federal Ministry of Education and Research (BMBF; grant no. 01DL20003).

Availability of data and materials

Data are available through the corresponding author upon grounded request.

Declarations

Ethics approval and consent to participate

The conducted animal study followed the international, and institutional guidelines for humane animal treatment and the study was approved by the institutional animal care and use committee of Kafrelsheikh University.

Consent for publication

Not applicable.

Competing interests

The authors declare that they have no competing interests.

Received: 6 February 2023 Accepted: 2 June 2023
Published online: 01 July 2023

References

Abdel Gaber SA (2017) Photodynamic diagnosis and therapy for oral potentially malignant disorders and cancers. In: Al Moustafa A-E (ed) Development of oral cancer: risk factors and prevention strategies, pp 147–175. Springer, Cham. https://doi.org/10.1007/978-3-319-48054-1_10

Abdel Gaber SA, Fadel M. Nanotechnology and photodynamic therapy from a clinical perspective. Transl. Biophotonics 2023 Mar 1;5(1):e202200016. Available from: https://doi.org/10.1002/tbio.202200016

Abdel Gaber SA, Müller P, Zimmermann W, Hüttenberger D, Wittig R, Abdel Kader MH, Stepp H (2018) ABCG2-mediated suppression of chlorin e6 accumulation and photodynamic therapy efficiency in glioblastoma cell lines can be reversed by KO143. J Photochem Photobiol B Biol 178:182–191. https://doi.org/10.1016/j.jphotobiol.2017.10.035

Abdel Khalek MA, Abdel Gaber SA, El-Domany RA, El-Kemary MA (2021) Photoactive electrospun cellulose acetate/polyethylene oxide/methylene blue and trilayered cellulose acetate/polyethylene oxide/silk fibroin/ciprofloxacin nanofibers for chronic wound healing. Int J Biol Macromol 193:1752–1766. https://doi.org/10.1016/j.ijbiomac.2021.11.012

Aboelmaati MG, Abdel Gaber SA, Soliman WE, Elkhatib WF, Abdelhameed AM, Sahyon HA, El-Kemary M (2021) Biogenic and biocompatible silver nanoparticles for an apoptotic anti-ovarian activity and as polydopamine-functionalized antibiotic carrier for an augmented antibiofilm activity. Colloids Surf B Biointerfaces. https://doi.org/10.1016/J.COLSURFB.2021.111935

Al-Khaza'leh KA, Omar K, Jaafar MS (2011) pH effect on cellular uptake of Sn(IV) chlorine e6 dichloride trisodium salt by cancer cells in vitro. J Biol Phys 37(1):153–161. https://doi.org/10.1007/s10867-010-9206-4

Ali-Seyed M, Bhuvaneswari R, Soo Chee K, Olivo M (2011) Photolon™ - photosensitization induces apoptosis via ROS-mediated cross-talk between mitochondria and lysosomes. Int J Oncol 39(4):821–831. https://doi.org/10.3892/ijo.2011.1109

Barros ACSD, Muranaka ENK, Mori LJ, Pelizon CHT, Iriya K, Giocondo G, Pinotti JA (2004) Induction of experimental mammary carcinogenesis in rats with 7,12-dimethylbenz(a)anthracene. Rev Hosp Clín 59(5):257–261. https://doi.org/10.1590/s0041-87812004000500006

Bharathiraja S, Moorthy MS, Manivasagan P, Seo H, Lee KD, Oh J (2017) Chlorin e6 conjugated silica nanoparticles for targeted and effective photodynamic therapy. Photodiagnosis Photodyn Ther 19:212–220. https://doi.org/10.1016/j.pdpdt.2017.06.001

Cabral ÁS, Leonel ECR, Candido NM, Piva HL, de Melo MT, Taboga SR, Rahal P, Tedesco AC, Calmon MF (2021) Combined photodynamic therapy with chloroaluminum phthalocyanine and doxorubicin nanoemulsions in breast cancer model. J Photochem Photobiol B Biol 218:112181. https://doi.org/10.1016/j.jphotobiol.2021.112181

Chin WWL, Heng PWS, Thong PSP, Bhuvaneswari R, Hirt W, Kuenzel S, Soo KC, Olivo M (2008) Improved formulation of photosensitizer chlorin e6 polyvinylpyrrolidone for fluorescence diagnostic imaging and photodynamic therapy of human cancer. Eur J Pharm Biopharm 69(3):1083–1093. https://doi.org/10.1016/j.ejpb.2008.02.013

Couleaud P, Morosini V, Frochot C, Richeter S, Raehm L, Durand J-O (2010) Silica-based nanoparticles for photodynamic therapy applications. Nanoscale 2(7):1083–1095. https://doi.org/10.1039/C0NR00096E

El-Gogary RI, Abdel Gaber SA, Nasr M (2019) Polymeric nanocapsular baicalin: chemometric optimization, physicochemical characterization and mechanistic anticancer approaches on breast cancer cell lines. Sci Rep 9(1):1–14. https://doi.org/10.1038/s41598-019-47586-7

Etienne M, Walcarius A (2003) Analytical investigation of the chemical reactivity and stability of aminopropyl-grafted silica in aqueous medium. Talanta 59(6):1173–1188. https://doi.org/10.1016/S0039-9140(03)00024-9

Feng C, Zhu D, Chen L, Lu Y, Liu J, Kim NY, Liang S, Zhang X, Lin Y, Ma Y, Dong C (2019) Targeted delivery of chlorin e6 via redox sensitive diselenide-containing micelles for improved photodynamic therapy in cluster of differentiation 44-overexpressing breast cancer. Front Pharmacol 10:369. https://doi.org/10.3389/fphar.2019.00369

Fukuhara H, Inoue K, Kurabayashi A, Furihata M, Fujita H, Utsumi K, Sasaki J, Shuin T (2013) The inhibition of ferrochelatase enhances 5-aminolevulinic acid-based photodynamic action for prostate cancer. Photodiagnosis Photodyn Ther 10(4):399–409. https://doi.org/10.1016/j.pdpdt.2013.03.003

Gaio E, Guerrini A, Ballestri M, Varchi G, Ferroni C, Martella E, Columbaro M, Moret F, Reddi E (2019) Keratin nanoparticles co-delivering docetaxel and chlorin e6 promote synergic interaction between chemo- and photo-dynamic therapies. J Photochem Photobiol B Biol 199:111598. https://doi.org/10.1016/j.jphotobiol.2019.111598

Guney Eskiler G, Deveci Ozkan A, Sozen Kucukkara E, Kamanlı AF, Gunoğlu B, Yıldız MZ (2020) Optimization of 5-aminolevulinic acid-based photodynamic therapy protocol for breast cancer cells. Photodiagnosis Photodyn Ther 31:101854. https://doi.org/10.1016/j.pdpdt.2020.101854

Hädener M, Gjuroski I, Furrer J, Vermathen M (2015) Interactions of polyvinylpyrrolidone with chlorin e6-based photosensitizers studied by NMR and electronic absorption spectroscopy. J Phys Chem B 119(36):12117–12128. https://doi.org/10.1021/acs.jpcb.5b05761

Heuts J, Jiskoot W, Ossendorp F, van der Maaden K (2021) Cationic nanoparticle-based cancer vaccines. Pharmaceutics 13(5):596. https://doi.org/10.3390/pharmaceutics13050596

Hüttenberger D, Simon C, Mohrbacher C, Betz N, Bauer-Marschall I, Stachon A, Giesen T, Foth H-J (2017) Photodynamic inactivation of *Helicobacter pylori* with chlorin e6 trisodium salt—a new approach against a widespread disease. Photodiagnosis Photodyn Ther 17:A12–A13. https://doi.org/10.1016/j.pdpdt.2017.01.029

Isakau HA, Parkhats MV, Knyukshto VN, Dzhagarov BM, Petrov EP, Petrov PT (2008) Toward understanding the high PDT efficacy of chlorin e6–polyvinylpyrrolidone formulations: photophysical and molecular aspects of photosensitizer–polymer interaction in vitro. J Photochem Photobiol B Biol 92(3):165–174. https://doi.org/10.1016/j.jphotobiol.2008.06.004

Jambhrunkar S, Qu Z, Popat A, Yang J, Noonan O, Acauan L, Ahmad Nor Y, Yu C, Karmakar S (2014) Effect of surface functionality of silica nanoparticles on cellular uptake and cytotoxicity. Mol Pharm 11(10):3642–3655. https://doi.org/10.1021/mp500385n

Jeong H, Huh M, Lee SJ, Koo H, Kwon IC, Jeong SY, Kim K (2011) Photosensitizer-conjugated human serum albumin nanoparticles for effective photodynamic therapy. Theranostics 1:230–239. https://doi.org/10.7150/thno/v01p0230

Kammerer R, Buchner A, Palluch P, Pongratz T, Oboukhovskij K, Beyer W, Johansson A, Stepp H, Baumgartner R, Zimmermann W (2011) Induction of immune mediators in glioma and prostate cancer cells by non-lethal photodynamic therapy. PLoS ONE 6(6):e21834. https://doi.org/10.1371/journal.pone.0021834

Kim Y-J, Lee H-I, Kim J-K, Kim C-H, Kim Y-J (2020) Peptide 18–4/chlorin e6-conjugated polyhedral oligomeric silsesquioxane nanoparticles for targeted photodynamic therapy of breast cancer. Colloids Surf B Biointerfaces 189:110829. https://doi.org/10.1016/j.colsurfb.2020.110829

Kobayashi T, Nitta M, Shimizu K, Saito T, Tsuzuki S, Fukui A, Koriyama S, Kuwano A, Komori T, Masui K, Maehara T, Kawamata T, Muragaki Y (2022) Therapeutic options for recurrent glioblastoma-efficacy of talaporfin sodium mediated photodynamic therapy. Pharmaceutics 14(2):353. https://doi.org/10.3390/pharmaceutics14020353

Kumari P, Rompicharla SVK, Bhatt H, Ghosh B, Biswas S (2019) Development of chlorin e6-conjugated poly(ethylene glycol)-poly(d, l-lactide) nanoparticles for photodynamic therapy. Nanomedicine 14(7):819–834. https://doi.org/10.2217/nnm-2018-0255

Lee J, Lee YM, Kim J, Kim WJ (2017) Doxorubicin/Ce6-loaded nanoparticle coated with polymer via singlet oxygen-sensitive linker for photodynamically assisted chemotherapy. Nanotheranostics 1(2):196–207. https://doi.org/10.7150/ntno.18576

Lin C-Y, Yang C-M, Lindén M (2019) Influence of serum concentration and surface functionalization on the protein adsorption to mesoporous silica nanoparticles. RSC Adv 9(58):33912–33921. https://doi.org/10.1039/C9RA05585A

Lin C-Y, Yang C-M, Lindén M (2022) Dissolution and morphology evolution of mesoporous silica nanoparticles under biologically relevant conditions. J Colloid Interface Sci 608:995–1004. https://doi.org/10.1016/j.jcis.2021.09.164

Mamaeva V, Rosenholm JM, Bate-Eya LT, Bergman L, Peuhu E, Duchanoy A, Fortelius LE, Landor S, Toivola DM, Lindén M, Sahlgren C (2011) Mesoporous silica nanoparticles as drug delivery systems for targeted inhibition of notch signaling in cancer. Mol Ther 19(8):1538–1546. https://doi.org/10.1038/mt.2011.105

Mamaeva V, Sahlgren C, Lindén M (2013) Mesoporous silica nanoparticles in medicine—recent advances. Adv Drug Deliv Rev 65(5):689–702. https://doi.org/10.1016/j.addr.2012.07.018

Mfouo-Tynga IS, Dias LD, Inada NM, Kurachi C (2021) Features of third generation photosensitizers used in anticancer photodynamic therapy: review. Photodiagnosis Photodyn Ther 34:102091. https://doi.org/10.1016/j.pdpdt.2020.102091

Mojzisova H, Bonneau S, Vever-Bizet C, Brault D (2007a) Cellular uptake and subcellular distribution of chlorin e6 as functions of pH and interactions with membranes and lipoproteins. Biochim Biophys Acta Biomembr 1768(11):2748–2756. https://doi.org/10.1016/j.bbamem.2007.07.002

Mojzisova H, Bonneau S, Vever-Bizet C, Brault D (2007b) The pH-dependent distribution of the photosensitizer chlorin e6 among plasma proteins and membranes: a physico-chemical approach. Biochim Biophys Acta Biomembr 1768(2):366–374. https://doi.org/10.1016/j.bbamem.2006.10.009

Möller K, Bein T (2019) Degradable drug carriers: vanishing mesoporous silica nanoparticles. Chem Mater 31(12):4364–4378. https://doi.org/10.1021/acs.chemmater.9b00221

Müller P, Abdel Gaber SA, Zimmermann W, Wittig R, Stepp H (2020) ABCG2 influence on the efficiency of photodynamic therapy in glioblastoma cells. J Photochem Photobiol B Biol 210:111963–111971. https://doi.org/10.1016/j.jphotobiol.2020.111963

Nicotera P, Melino G (2004) Regulation of the apoptosis–necrosis switch. Oncogene 23(16):2757–2765. https://doi.org/10.1038/sj.onc.1207559

Ozten O, Guney Eskiler G, Sonmez F, Yıldız MZ (2022) Investigation of the therapeutic effect of 5-aminolevulinic acid based photodynamic therapy on hepatocellular carcinoma. Lasers Med Sci 37(2):1325–1332. https://doi.org/10.1007/s10103-021-03398-8

Panariti A, Miserocchi G, Rivolta I (2012) The effect of nanoparticle uptake on cellular behavior: disrupting or enabling functions? Nanotechnol Sci Appl 5:87–100. https://doi.org/10.2147/NSA.S25515

Peng Q, Warloe T, Berg K, Moan J, Kongshaug M, Giercksky K-E, Nesland JM (1997) 5-Aminolevulinic acid-based photodynamic therapy. Cancer 79(12):2282–2308. https://doi.org/10.1002/(SICI)1097-0142(19970615)79:12%3c2282::AID-CNCR2%3e3.0.CO;2-O

Pinto B, Henriques AC, Silva PMA, Bousbaa H (2020) Three-dimensional spheroids as in vitro preclinical models for cancer research. Pharmaceutics 12(12):1186. https://doi.org/10.3390/pharmaceutics12121186

Rosenholm JM, Meinander A, Peuhu E, Niemi R, Eriksson JE, Sahlgren C, Lindén M (2009) Targeting of porous hybrid silica nanoparticles to cancer cells. ACS Nano 3(1):197–206. https://doi.org/10.1021/nn800781r

Simon C, Mohrbacher C, Hüttenberger D, Bauer-Marschall I, Krickhahn C, Stachon A, Foth H-J (2014) In vitro studies of different irradiation conditions for photodynamic inactivation of *Helicobacter pylori*. J Photochem Photobiol B Biol 141:113–118. https://doi.org/10.1016/j.jphotobiol.2014.09.015

Song Y, Tan X, Gao Y (2022) Platelet-biomimetic nanoparticles for in vivo targeted photodynamic therapy of breast cancer. Biomater Sci Polymer Ed 33(11):1383–1397. https://doi.org/10.1080/09205063.2022.2056942

Su J, Sun H, Meng Q, Zhang P, Yin Q, Li Y (2017) Enhanced blood suspensibility and laser-activated tumor-specific drug release of theranostic mesoporous silica nanoparticles by functionalizing with erythrocyte membranes. Theranostics 7(3):523–537. https://doi.org/10.7150/thno.17259

Teng L, Nakada M, Zhao S-G, Endo Y, Furuyama N, Nambu E, Pyko IV, Hayashi Y, Hamada J-I (2011) Silencing of ferrochelatase enhances 5-aminolevulinic acid-based fluorescence and photodynamic therapy efficacy. Br J Cancer 104(5):798–807. https://doi.org/10.1038/bjc.2011.12

Wang H-X, Zuo Z-Q, Du J-Z, Wang Y-C, Sun R, Cao Z-T, Ye X-D, Wang J-L, Leong KW, Wang J (2016) Surface charge critically affects tumor penetration and therapeutic efficacy of cancer nanomedicines. Nano Today 11(2):133–144. https://doi.org/10.1016/j.nantod.2016.04.008

Wang L, Wang L, Zhang Y, Zhao Z, Liu C, Li M, Liu J, Wang S, Yang D, Luo F, Yan J (2022) LS-HB-mediated photodynamic therapy inhibits proliferation and induces cell apoptosis in melanoma. Mol Pharm 19(7):2607–2619. https://doi.org/10.1021/acs.molpharmaceut.2c00302

Wawrzyńska M, Kałas W, Biały D, Zioło E, Arkowski J, Mazurek W, Strządała L (2010) In vitro photodynamic therapy with chlorin e6 leads to apoptosis of human vascular smooth muscle cells. Arch Immunol Ther Exp 58(1):67–75. https://doi.org/10.1007/s00005-009-0054-5

Winkler K, Simon C, Finke M, Bleses K, Birke M, Szentmáry N, Hüttenberger D, Eppig T, Stachon T, Langenbucher A, Foth H-J, Herrmann M, Seitz B, Bischoff M (2016) Photodynamic inactivation of multidrug-resistant *Staphylococcus aureus* by chlorin e6 and red light (λ=670nm). J Photochem Photobiol B Biol 162:340–347. https://doi.org/10.1016/j.jphotobiol.2016.07.007

Wittig R, Rosenholm JM, von Haartman E, Hemming J, Genze F, Bergman L, Simmet T, Lindén M, Sahlgren C (2013) Active targeting of mesoporous silica drug carriers enhances γ-secretase inhibitor efficacy in an in vivo model for breast cancer. Nanomedicine 9(7):971–987. https://doi.org/10.2217/nnm.13.62

Wu M-F, Deichelbohrer M, Tschernig T, Laschke MW, Szentmáry N, Hüttenberger D, Foth H-J, Seitz B, Bischoff M (2017) Chlorin e6 mediated photodynamic inactivation for multidrug resistant *Pseudomonas aeruginosa* keratitis in mice in vivo. Sci Rep 7(1):44537. https://doi.org/10.1038/srep44537

Xiao H, Zhu B, Wang D, Pang Y, He L, Ma X, Wang R, Jin C, Chen Y, Zhu X (2012) Photodynamic effects of chlorin e6 attached to single wall carbon nanotubes through noncovalent interactions. Carbon 50(4):1681–1689. https://doi.org/10.1016/j.carbon.2011.12.013

Xu C, Nam J, Hong H, Xu Y, Moon JJ (2019) Positron emission tomography-guided photodynamic therapy with biodegradable mesoporous silica nanoparticles for personalized cancer immunotherapy. ACS Nano 13(10):12148–12161. https://doi.org/10.1021/acsnano.9b06691

Yano T, Minamide T, Takashima K, Nakajo K, Kadota T, Yoda Y (2021) Clinical practice of photodynamic therapy using talaporfin sodium for esophageal cancer. J Clin Med 10(13):2785. https://doi.org/10.3390/jcm10132785

Yasin G, Nasr M, Abdel Gaber SA, Hüttenberger D, Fadel M (2022) Response surface methodological approach for optimization of photodynamic therapy of onychomycosis using chlorin e6 loaded nail penetration enhancer vesicles. J Photochem Photobiol B Biol 232:112461. https://doi.org/10.1016/j.jphotobiol.2022.112461

Youssef Z, Jouan-Hureaux V, Colombeau L, Arnoux P, Moussaron A, Baros F, Toufaily J, Hamieh T, Roques-Carmes T, Frochot C (2018) Titania and silica nanoparticles coupled to chlorin e6 for anti-cancer photodynamic therapy. Photodiagnosis Photodyn Ther 22:115–126. https://doi.org/10.1016/j.pdpdt.2018.03.005

Yu Z, Xiao Z, Shuai X, Tian J (2020) Local delivery of sunitinib and Ce6 via redox-responsive zwitterionic hydrogels effectively prevents osteosarcoma recurrence. J Mater Sci Eng B 8(30):6418–6428. https://doi.org/10.1039/d0tb00970a

Zeng L, Li W, Chen C-S (2020) Breast cancer animal models and applications. Zool Res 41(5):477–494. https://doi.org/10.24272/j.issn.2095-8137.2020.095

Publisher's Note